

# Ab initio real-time quantum dynamics of charge carriers in momentum space

Received: 9 November 2022

Accepted: 21 April 2023

Published online: 1 June 2023

 Check for updates

Zhenfa Zheng  <sup>1</sup>, Yongliang Shi  <sup>1,2,3</sup> , Jin-Jian Zhou<sup>4</sup>, Oleg V. Prezhdo<sup>5</sup>, Qijing Zheng  <sup>1</sup> & Jin Zhao  <sup>1,6,7</sup> 

Application of the non-adiabatic molecular dynamics (NAMD) approach is limited to studying carrier dynamics in the momentum space, as a supercell is required to sample the phonon excitation and electron–phonon (e–ph) interaction at different momenta in a molecular dynamics simulation. Here we develop an ab initio approach for the real-time charge carrier quantum dynamics in the momentum space (NAMD  $\mathbf{k}$ ) by directly introducing e–ph coupling into the Hamiltonian based on the harmonic approximation. The NAMD  $\mathbf{k}$  approach maintains the zero-point energy and includes memory effects of carrier dynamics. The application of NAMD  $\mathbf{k}$  to the hot carrier dynamics in graphene reveals the phonon-specific relaxation mechanism. An energy threshold of 0.2 eV—defined by two optical phonon modes—separates the hot electron relaxation into fast and slow regions with lifetimes of pico- and nanoseconds, respectively. The NAMD  $\mathbf{k}$  approach provides an effective tool to understand real-time carrier dynamics in the momentum space for different materials.

Tracking the quantum dynamics of excited charge carriers in solid materials in multidimensions—including time and energy domains, as well as real and momentum spaces—is fundamental to understanding many dynamical processes in optoelectronics, spin- and valleytronics, solar energy conversion and so on<sup>1–3</sup>. Different experimental techniques—including ultrafast time- and angle-resolved photoemission spectroscopy (TR-ARPES), with time, energy and momentum resolution—have been rapidly developed and applied to investigate charge carrier dynamics in various materials<sup>4</sup>. However, without the input of ab initio investigations, it is difficult to understand the physical mechanisms behind the experimental spectra. It is therefore urgent to develop an ab initio simulation approach to achieve a state-of-the-art understanding of multidimensional carrier dynamics in solids.

An ab initio approach based on perturbation theory provides useful information to understand carrier lifetimes governed by different

scattering mechanisms<sup>5</sup>. In the past few years, the development of the real-time Boltzmann transport equation (rt-BTE) made it possible to investigate the carrier and phonon dynamics based on the semi-classical Boltzmann transport equation<sup>6–8</sup>. On the other hand, in recent decades, real-time time-dependent density functional theory (rt-TDDFT), which is based on Ehrenfest dynamics<sup>9–15</sup>, and non-adiabatic molecular dynamics (NAMD) approaches, which combines real-time time-dependent Kohn–Sham theory and surface hopping, have been applied to investigate the quantum dynamics of excited charge carriers in a non-perturbative way<sup>3,16–19</sup>. Electron–phonon (e–ph) coupling, spin–orbit coupling (SOC) and the many-body electron–hole interaction have been included with different theoretical strategies<sup>20–25</sup>; however, it is difficult to achieve real-time carrier dynamics in the momentum space in all of these methods. In past NAMD simulations, the phonon excitation is described using ab initio molecular dynamics (AIMD) within periodic boundary conditions, and only phonons at the

<sup>1</sup>Department of Physics, ICQD/Hefei National Research Center for Physical Sciences at the Microscale, University of Science and Technology of China, Hefei, China. <sup>2</sup>Center for Spintronics and Quantum Systems, State Key Laboratory for Mechanical Behavior of Materials, School of Materials Science and Engineering, Xi'an Jiaotong University, Xi'an, China. <sup>3</sup>State Key Laboratory of Surface Physics and Department of Physics, Fudan University, Shanghai, China. <sup>4</sup>School of Physics, Beijing Institute of Technology, Beijing, China. <sup>5</sup>Departments of Chemistry, Physics, and Astronomy, University of Southern California, Los Angeles, CA, USA. <sup>6</sup>Department of Physics and Astronomy, University of Pittsburgh, Pittsburgh, PA, USA. <sup>7</sup>Hefei National Laboratory, University of Science and Technology of China, Hefei, China.  e-mail: [sycliff@xjtu.edu.cn](mailto:sycliff@xjtu.edu.cn); [zqj@ustc.edu.cn](mailto:zqj@ustc.edu.cn); [zhaojin@ustc.edu.cn](mailto:zhaojin@ustc.edu.cn)

$\Gamma$  point (the centre of the Brillouin zone where the momentum is zero) are included. The electron transition from one  $\mathbf{k}$ -point (a point in the reciprocal space representing the momentum of the electron) to another through e-ph is therefore forbidden even though the electronic states can be simulated using multiple  $\mathbf{k}$ -points. To sample the phonon excitation and electron–phonon interaction at different momenta, a supercell needs to be used so that phonons at other  $\mathbf{q}$ -points (points in the reciprocal space representing the momenta of phonon modes) can be folded to the  $\Gamma$  point. The density of the  $\mathbf{q}$ -point grid is determined by the size of the supercell and, due to the computational cost, usually only a few  $\mathbf{q}$ -points can be included in the NAMD simulation<sup>3,20,22</sup>. By contrast, the e-ph scattering between different momenta often needs to be simulated with very dense  $\mathbf{k}$ - and  $\mathbf{q}$ -point grids, especially when the electronic band dispersion is strong. An ab initio approach to describe the real-time quantum dynamics of photo-excited carriers in the momentum space is thus essential.

In this work, by introducing e-ph coupling elements into the time-propagation Hamiltonian, we extended the ab initio NAMD approach from the real-space (NAMD\_r) to the momentum space (NAMD\_k). Unlike the NAMD\_r approach, in which a large supercell AIMD simulation is required for  $\mathbf{q}$ -grid sampling, in NAMD\_k,  $\mathbf{k}$  and  $\mathbf{q}$  sampling is performed by the calculation of e-ph matrix elements using a unit cell; the computational cost is therefore substantially reduced. Moreover, the NAMD\_k approach provides a straightforward picture not only of the dynamics of excited electrons in the momentum space, but also the time-dependent phonon excitation of the lattice due to the e-ph scattering. The phonon zero-point energy and phonon dispersion are accurately represented with memory effects. Using this approach, we have investigated the hot carrier dynamics in graphene. It is found that there is an energy threshold at 0.2 eV above the Fermi level ( $E_F$ ). The threshold separates the hierarchical relaxation dynamics from fast (picosecond) to slow (nanosecond) regions. The intervalley e-ph scattering is activated in the fast region but strongly suppressed in the slow region. The energy threshold is determined by strongly coupled optical phonon modes  $A_1$  and  $E_{2g}$ . Our work not only reveals the phonon mode-specific energy threshold for hot electron relaxation in graphene, but also provides a tool which can be widely applied to study excited carrier dynamics in different solid state systems with momentum space resolution.

## Results

### Theoretical framework of NAMD\_k

In the NAMD\_r approach, the charge carrier (electron or hole) wavefunction  $|\Psi(\mathbf{r}; \mathbf{R}(t))\rangle$  is expanded in the basis of instantaneous adiabatic Kohn–Sham orbitals  $|\psi_n(\mathbf{r}; \mathbf{R}(t))\rangle$ , which are obtained by solving the Kohn–Sham equation at atomic configuration  $\mathbf{R}(t)$ ,

$$|\Psi(\mathbf{r}; \mathbf{R}(t))\rangle = \sum_n c_n(t) |\psi_n(\mathbf{r}; \mathbf{R}(t))\rangle, \quad (1)$$

where  $c_n(t)$  is the time-dependent expansion coefficient of the  $n$ th Kohn–Sham orbital, and  $\mathbf{r}$  is the position of carrier. Based on the classical-path approximation (CPA)<sup>16</sup>,  $\mathbf{R}(t)$  can be obtained by AIMD. The charge carrier wavefunction follows the time-dependent Schrödinger equation (TDSE)

$$i\hbar \frac{\partial}{\partial t} |\Psi(\mathbf{r}; \mathbf{R}(t))\rangle = \hat{H}^{\text{el}}(\mathbf{r}; \mathbf{R}(t)) |\Psi(\mathbf{r}; \mathbf{R}, t)\rangle, \quad (2)$$

where  $\hat{H}^{\text{el}}$  is the electronic Hamiltonian. Then, a set of differential equations for the coefficients  $c_m(t)$  is produced

$$i\hbar \dot{c}_m(t) = \sum_n c_n(t) [\epsilon_n - i\hbar d_{mn}], \quad (3)$$

where  $\epsilon_n$  is the energy of the adiabatic Kohn–Sham state, and  $d_{mn}$  is the non-adiabatic coupling (NAC) between Kohn–Sham states  $m$  and  $n$ . The NAC can be written as

$$d_{mn} = \langle \psi_m | \frac{d}{dt} |\psi_n\rangle = \frac{\langle \psi_m | \nabla_{\mathbf{R}} \hat{H}^{\text{el}} | \psi_n \rangle}{\epsilon_n - \epsilon_m} \cdot \dot{\mathbf{R}}. \quad (4)$$

Here,  $\epsilon_m$  and  $\epsilon_n$  are the eigenvalues of the Kohn–Sham orbitals  $m$  and  $n$ ,  $d_{mn}$  is the e-ph coupling term, and  $\dot{\mathbf{R}}$  is the nuclear velocity; NAC is the crucial term in the NAMD\_r simulation. It determines not only the time-dependent coefficient evolution, but also the hopping probability in the subsequent surface hopping step<sup>16,17</sup>. According to Bloch's theory, NAC is zero if  $\psi_m$  and  $\psi_n$  have different  $\mathbf{k}$  vectors (see Supplementary Section 1 for more details); therefore, the NAMD\_r approach cannot efficiently simulate the carrier dynamics in the momentum space.

The NAMD\_k approach is based on the harmonic approximation. By contrast with equation (1), we expand the charge carrier wavefunction using the Kohn–Sham orbitals of the equilibrium atomic configuration  $\mathbf{R}_0$

$$|\Psi(\mathbf{r}; \mathbf{R}(t))\rangle = \sum_{n\mathbf{k}} c_{n\mathbf{k}}(t) |\psi_{n\mathbf{k}}(\mathbf{r}; \mathbf{R}_0)\rangle, \quad (5)$$

where the Kohn–Sham orbital  $|\psi_{n\mathbf{k}}(\mathbf{r}; \mathbf{R}_0)\rangle$ , with band index  $n$  and momentum  $\mathbf{k}$ , is the eigenstate of the equilibrium configuration  $\mathbf{R}_0$ . The charge carrier Hamiltonian is naturally divided into two parts:

$$\hat{H}^{\text{el}}(\mathbf{r}; \mathbf{R}(t)) = \hat{H}^0(\mathbf{r}; \mathbf{R}_0) + \Delta V(\mathbf{r}; \mathbf{R}(t)), \quad (6)$$

where  $\Delta V$  is the variation of the potential induced by nuclear displacements  $\Delta \mathbf{R}(t) = \mathbf{R}(t) - \mathbf{R}_0$ . Combining the above equations, we get a new coefficient evolution equation:

$$i\hbar \frac{d}{dt} c_{m\mathbf{k}'}(t) = \sum_{n\mathbf{k}} (H_{m\mathbf{k}', n\mathbf{k}}^0 + H_{m\mathbf{k}', n\mathbf{k}}^{\text{e-ph}}) c_{n\mathbf{k}}(t). \quad (7)$$

Here,

$$H_{m\mathbf{k}', n\mathbf{k}}^0 = \langle \psi_{m\mathbf{k}'} | \hat{H}^0 | \psi_{n\mathbf{k}} \rangle = \epsilon_{n\mathbf{k}} \delta_{mn} \delta_{\mathbf{k}'\mathbf{k}}, \quad (8)$$

is the diagonal Kohn–Sham energy matrix and

$$H_{m\mathbf{k}', n\mathbf{k}}^{\text{e-ph}} = \langle \psi_{m\mathbf{k}'} | \Delta V | \psi_{n\mathbf{k}} \rangle, \quad (9)$$

is the e-ph coupling Hamiltonian;  $m$  and  $n$  denote the Kohn–Sham orbitals, whereas  $\mathbf{k}$  and  $\mathbf{k}'$  denote the momentum.

Transformed into the momentum space (see the Methods for a detailed derivation), the e-ph term can be rewritten as

$$\begin{aligned} H_{m\mathbf{k}', n\mathbf{k}}^{\text{e-ph}} &= \frac{1}{\sqrt{N}} \sum_{\mathbf{q}\mathbf{v}} \langle u_{m\mathbf{k}'} | \Delta_{\mathbf{q}\mathbf{v}} v(\mathbf{r}; \mathbf{R}_0) | u_{n\mathbf{k}} \rangle_{uc} \delta_{\mathbf{q}, \mathbf{k}' - \mathbf{k}} Q_{\mathbf{q}\mathbf{v}}(t) / l_{\mathbf{q}\mathbf{v}} \\ &= \frac{1}{\sqrt{N}} \sum_{\mathbf{v}} g_{mn\mathbf{v}}(\mathbf{k}, \mathbf{q}) Q_{\mathbf{q}\mathbf{v}}(t) / l_{\mathbf{q}\mathbf{v}}|_{\mathbf{q}=\mathbf{k}'-\mathbf{k}}, \end{aligned} \quad (10)$$

where  $N$  is the number of unit cells according to the Born–von Kármán boundary conditions,  $Q_{\mathbf{q}\mathbf{v}}(t)$  is the normal mode coordinate of the corresponding vibration mode of a phonon with momentum  $\mathbf{q}$  in branch  $\mathbf{v}$ ,  $l_{\mathbf{q}\mathbf{v}}$  is the zero-point displacement amplitude, and  $g_{mn\mathbf{v}}(\mathbf{k}, \mathbf{q})$  is the e-ph matrix element. In this way, the NAC in the NAMD\_r approach is replaced by the e-ph coupling Hamiltonian in equation (10), which naturally includes the coupling between electronic states with different momenta  $\mathbf{k}$ , and the scattering with phonons at different momenta  $\mathbf{q}$ .

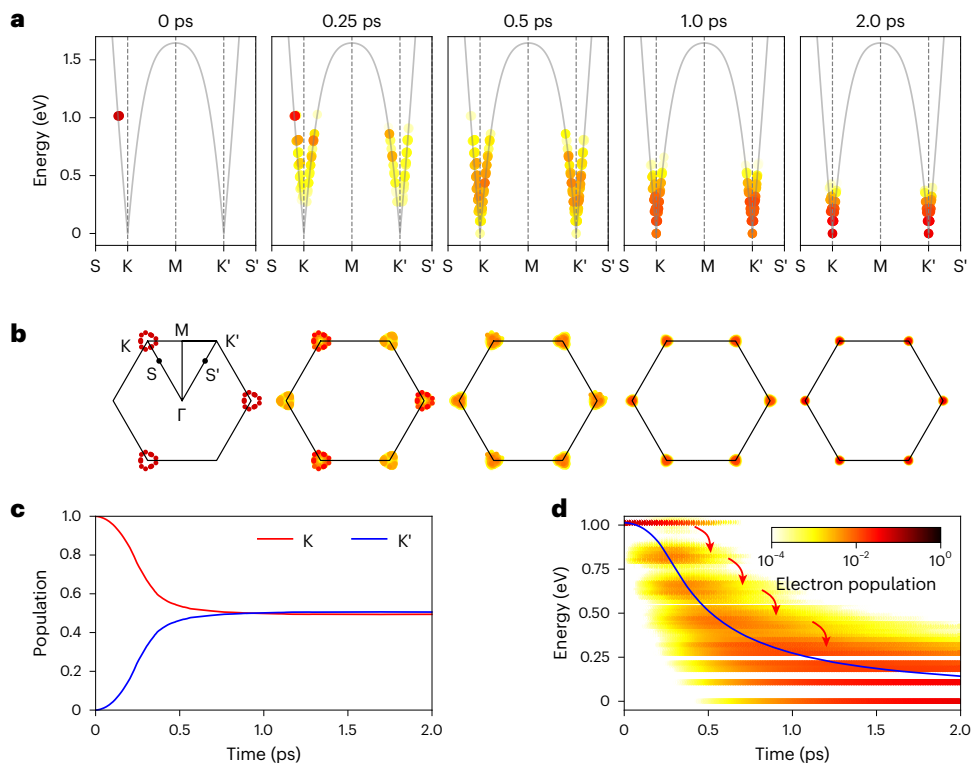


**Fig. 1 | Hot electron relaxation in graphene with  $E_{\text{ini}} = 1.0$  eV using  $150 \times 150 \times 1$ k-point grid.** **a,b**, Snapshots of hot electron population in energy (a) and in momentum space (b) at 0, 0.25, 0.5, 1.0 and 2.0 ps. **c**, Time-dependent normalized electron population in the K and K' valleys. Here,  $\Gamma$ , K, K' and M are high symmetry points in the first Brillouin zone, and their fractional coordinates are  $(0, 0, 0)$ ,  $(\frac{1}{3}, \frac{1}{3}, 0)$ ,  $(-\frac{1}{3}, \frac{2}{3}, 0)$  and  $(0, \frac{1}{2}, 0)$ , respectively; S and S' are  $\mathbf{k}$ -points on

$\Gamma$ K and  $\Gamma$ K' paths, and their fractional coordinates are  $(\frac{2}{9}, \frac{2}{9}, 0)$  and  $(-\frac{2}{3}, \frac{4}{9}, 0)$ , respectively. **d**, Hot electron relaxation in the energy domain. The colour bar indicates the electron population and the blue curve represents the averaged electron energy. The colored dots in **a**, **b** and **d** indicate the normalized electron population, and they share the same color bar as the one in **d**. The energy reference of **a** and **d** is the  $E_f$ .

To obtain the real-time carrier dynamics via the NAMD\_k method, the e-ph coupling matrix element  $g_{mnv}(\mathbf{k}, \mathbf{q})$  and the time-dependent normal mode coordinate  $Q_{qv}(t)$  need to be computed;  $g_{mnv}(\mathbf{k}, \mathbf{q})$  can be calculated by the density functional perturbation theory method using the primitive cell<sup>26</sup> or finite difference method with non-diagonal supercells<sup>27</sup>, whereas  $Q_{qv}(t)$  can be obtained using different methods. For example, it can be expressed in terms of phonon populations as

$$Q_{qv}(t) = I_{qv} \sqrt{n_{qv} + \frac{1}{2}} (e^{-i\omega_{qv}t} + e^{i\omega_{qv}t}), \quad (11)$$

where the initial population of phonons at  $t = 0$  ( $t_0$ ) is given by the Bose-Einstein distribution  $n_{qv} = \frac{1}{e^{\hbar\omega_{qv}/k_B T} - 1}$ . It can also be obtained from the molecular dynamics simulation by using the normal mode decomposition method<sup>28</sup>. The factor of one-half represents the zero-point energy contribution. Finally, fewest-switches surface hopping (FSSH) is applied to include the stochastic factor of the carrier dynamics. We use a 1 as timestep for the electron dynamics and a 1 fs timestep for the nuclear dynamics; thus the CPA is applied<sup>16</sup>. As the velocity of the atoms is much slower than the speed of light, the retarded time is not considered in the calculation<sup>29</sup>.

### Hot electron relaxation in graphene

We choose graphene as a prototypical system and simulate the hot electron relaxation process, as has been investigated extensively in past works<sup>8,30–35</sup>. Graphene has six Dirac cones near the  $E_f$  at the K and K' points in the first Brillouin zone—known as the six valleys (Fig. 1a,b). Hot electron relaxation may involve inter- and intravalley e-ph scattering. We first study dynamics with a single electron initially excited at 1.0 eV

above the  $E_f$  ( $E_{\text{ini}} = 1.0$  eV, where  $E_{\text{ini}}$  represents initial energy of the hot electron) in the K valley. To obtain statistics on the quantum behavior of the excited electron, we randomly set the initially excited electron at 30 different  $\mathbf{k}$ -points in the K valley with  $E_{\text{ini}} = 1.0$  eV. We sample  $2 \times 10^4$  trajectories for each  $\mathbf{k}$ -point. We find that a  $150 \times 150 \times 1$ k-point grid achieves well-converged results (the  $\mathbf{k}$ -point grid convergence details are presented in the Supplementary Fig. 1). Figure 1a shows five snapshots of the hot electron population in the band structure over 2 ps, whereas Fig. 1b gives the corresponding hot electron distribution in the first Brillouin zone. It can be seen that although the hot electron is initially excited in the K valley, the K-K' intervalley scattering starts almost immediately. Figure 1c presents the time-dependent electron population in the K and K' valleys. The valley lifetime ( $\tau_K$ )—which is defined as the timescale on which the equilibrium between K and K' is reached—is around 0.4 ps. The intervalley scattering suggests that the hot electron couples with phonons with large momentum. Figure 1d shows the hot electron energy relaxation. It can be seen that there is an energy threshold for hot electron relaxation located at around 0.2 eV above the  $E_f$ . Above the threshold energy, the relaxation is a relatively fast process, which corresponds to energy relaxation from 1.0 eV to around 0.2 eV within 2 ps. Using a Gaussian function, the lifetime for this fast energy relaxation ( $\tau_E$ ) can be estimated to be 0.56 ps. Furthermore, a quantized character with an energy difference of around 0.2 eV as indicated in Fig. 1d. Following the fast process, there happens a much slower relaxation process from 0.2 eV to the Dirac point. The timescale of the slow process is difficult to be estimated with a 2 ps simulation.

To further understand the slow relaxation process close to the  $E_f$ , we perform a 100 ps NAMD\_k simulation for hot electron relaxation

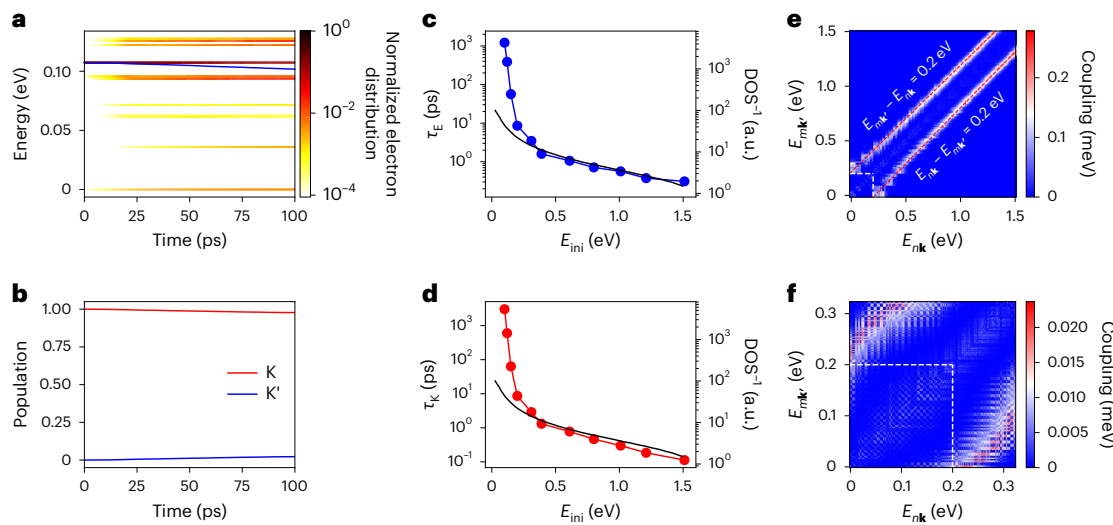


**Fig. 2 | Hot electron relaxation in graphene with different  $E_{\text{ini}}$ .** **a**, Hot electron relaxation in energy domain with  $E_{\text{ini}} = 0.1$  eV. The color strips indicate the normalized electron distribution in different energy states, and the blue line represents the averaged electron energy. The energy reference is the  $E_f$ . **b**, Time-dependent normalized electron population in the K and K' valleys with  $E_{\text{ini}} = 0.1$  eV. **c,d**, The dependence of  $\tau_E$  (**c**) and  $\tau_K$  (**d**) on  $E_{\text{ini}}$ . The black curves represent the reciprocal of the density of states (DOS $^{-1}$ ) at different energies. There are fast and slow processes in the electron relaxation. When  $E_{\text{ini}} > 0.2$  eV, the

electron relaxation is mainly governed by a fast process, whose relaxation time is proportional to the DOS $^{-1}$ . When  $E_{\text{ini}} < 0.2$  eV, the fast process is suppressed and the slow process remains. This results in a substantial increase in relaxation time. **e,f**, Coupling of e-ph, with the energy conservation factor (as shown in equation (27)) between states  $\psi_{mk'}$  and  $\psi_{nk}$  plotted with different  $E_{mk'}$  and  $E_{nk}$  scales. Here we used  $150 \times 150 \times 1\mathbf{k}$ -point grid for simulations with  $E_{\text{ini}} > 0.3$  eV, and  $450 \times 450 \times 1\mathbf{k}$ -point grid for simulations with  $E_{\text{ini}} < 0.3$  eV. The energy reference for each panel is the  $E_f$ .

with  $E_{\text{ini}} = 0.1$  eV. In this case, as the density of states (DOS) becomes smaller when the energy is close to the  $E_f$ , a more dense  $\mathbf{k}$ -point grid is required; we therefore use a  $450 \times 450 \times 1\mathbf{k}$ -point grid. The energy and valley dynamics are shown in Fig. 2a,b. As can be seen, both the energy and valley relaxation become much slower, and there is no longer a fast process in energy relaxation;  $\tau_E$  and  $\tau_K$  are estimated to be 1.2 and 3.0 ns, respectively. We further study the hot electron relaxation dynamics with different  $E_{\text{ini}}$  from 0.1 to 1.5 eV. As shown in Fig. 2c, it is found that  $E_{\text{ini}} = 0.2$  eV is a critical point for different relaxation behaviors. If  $E_{\text{ini}} > 0.2$  eV, there will be both a fast and a slow relaxation process. The  $\tau_E$  for the fast process ( $\tau_E^{\text{fast}}$ ) ranges from 0.3 to 3.0 ps, inversely proportional to the DOS. When  $E_{\text{ini}} < 0.2$  eV, there is only the slow process and  $\tau_E^{\text{slow}}$  dramatically increases by 1–3 orders of magnitude. The correlation between  $\tau_K$  and  $E_{\text{ini}}$  is shown in Fig. 2d, demonstrating a very similar trend with  $\tau_E$ . When  $E_{\text{ini}} < 0.2$  eV, the intervalley e-ph scattering becomes rare and  $\tau_K$  reaches a nanosecond timescale. The slow energy relaxation process is dominated by the intravalley scattering.

The e-ph coupling  $H_{mk',nk}^{e-ph} = \langle \psi_{mk'} | \Delta V | \psi_{nk} \rangle$  between states  $\psi_{mk'}$  and  $\psi_{nk}$  plays the key role in the NAMD\_K approach—analogous to the NAC in the NAMD\_r approach. In Fig. 2e,f we plot the averaged  $H_{mk',nk}^{e-ph}$ , where the x- and y-axes represent the energy of  $\psi_{mk'}$  and  $\psi_{nk}$  (labeled  $E_{mk'}$  and  $E_{nk}$ , respectively). In Fig. 2e, where  $E_{mk'}$  and  $E_{nk}$  range within (0.0, 1.5) eV, the largest  $H_{mk',nk}^{e-ph}$  can be roughly fitted by two lines, which are expressed as  $|E_{mk'} - E_{nk}| = 0.2$  eV, suggesting the coupling between two electronic states is the largest when the state energy difference is around 0.2 eV; thus, when  $E_{\text{ini}} > 0.2$  eV, the hot electron prefers to relax to an electronic state 0.2 eV lower in energy, which explains the quantized character with an energy difference of 0.2 eV observed in the fast relaxation process shown in Fig. 1d, suggesting that the hot electron relaxation is strongly coupled to phonons with energy of around 0.2 eV. The couplings between  $E_{mk'}$  and  $E_{nk}$  are much smaller when  $E_{\text{ini}} < 0.2$  eV, as indicated by the square marked with the white dashed lines in Fig. 2f. The matrix elements that are close to the diagonal line (where  $|E_{mk'} - E_{nk}|$  is very small) play a crucial role. This result implies that coupling to the phonons with small energies is essential in this case.

During the hot electron relaxation, the energy of the electrons transfers to the phonons through e-ph coupling. Figure 3 shows the phonon excitation dynamics along with the hot electron relaxation. Figure 3a shows the four snapshots of phonon excitation within 2 ps with  $E_{\text{ini}} = 1.0$  eV. It can be seen that only the optical modes  $A_1$  and  $E_{2g}$ —which belong to the longitudinal and transverse optical branches—are notably excited during the hot electron relaxation process. There is also a minor excitation for the longitudinal and transverse acoustic modes. Figure 3b,c shows the time-dependent phonon population and energies of these four different phonon modes. It can be seen that the excitations of the optical  $A_1$  and  $E_{2g}$  modes (with  $\hbar\omega_{A_1} = 0.16$  eV and  $\hbar\omega_{E_{2g}} = 0.19$  eV) are dominant. The excitation of  $A_1$  is responsible for the intervalley electron scattering, and both  $A_1$  and  $E_{2g}$  contribute to the quantized character in the energy relaxation process. Together, they define the critical energy threshold around 0.2 eV. Figure 3d–f presents the time-dependent phonon excitation with  $E_{\text{ini}} = 0.1$  eV. In this case, the longitudinal and transverse acoustic phonons excitation are dominant, as shown in Fig. 3d,e. The optical phonon mode  $A_1$  also has a minor contribution due to the thermal energy smearing of the electronic states (see Supplementary Section 4 for further details). As its energy is much higher than the longitudinal and transverse acoustic phonon energies, its contribution to the excited phonon energy is still dominant, as shown in Fig. 3f. As the energies and momenta of the longitudinal and transverse acoustic mode phonons are both very small, the energy and valley dynamics are much slower with  $E_{\text{ini}} = 0.1$  eV.

Finally, we study the multi-hot electron relaxation by simulating the electron temperature ( $T_e$ ) decrease. In the TR-ARPES measurements, after photoexcitation, the hot electrons will reach equilibrium with a certain temperature through electron-electron (e-e) scattering, and then relax to a lower temperature through e-ph coupling. Figure 4a shows five snapshots in the  $T_e$  relaxation with an initial electron temperature of  $T_e^{\text{ini}} = 3,193$  K. In this case  $T_e$  decreases to 639 K at 10 ps. Figure 4b shows the time-dependent relaxation dynamics with  $T_e^{\text{ini}} = 3,193, 2,200$  and  $1,060$  K. For all three cases,  $T_e$  converges to around 500 K at 10 ps. The relaxation from 500 K to lower temperature is very slow.

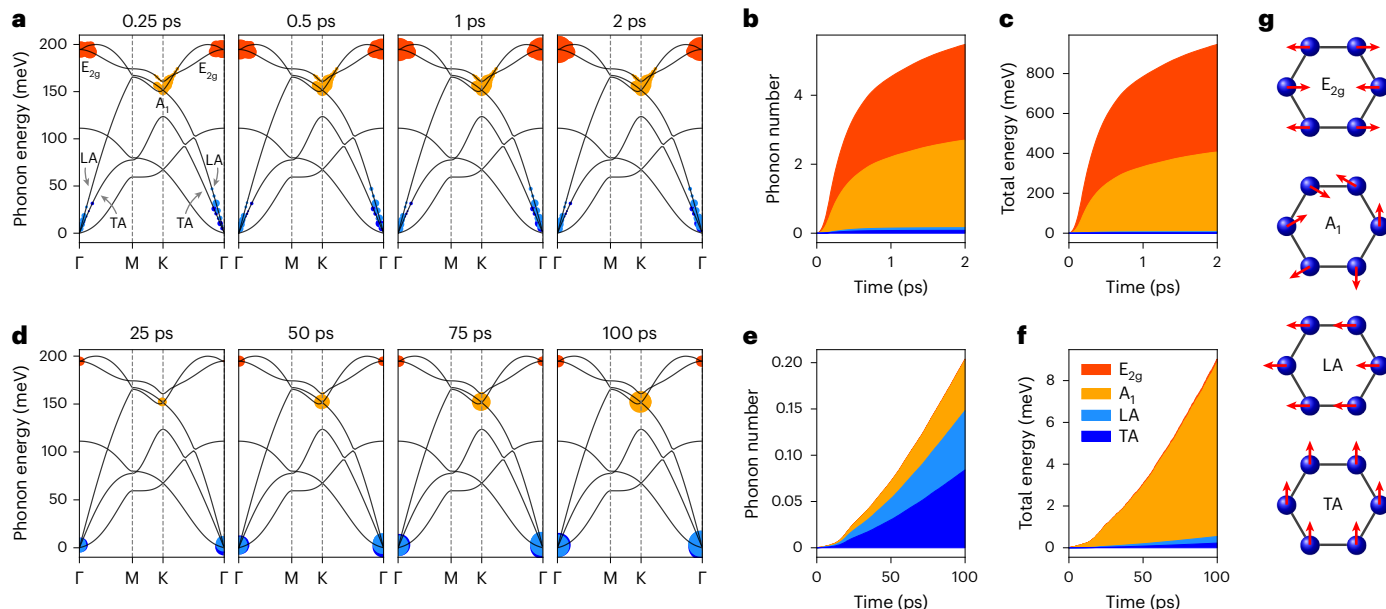


**Fig. 3 | Time-dependent phonon excitation during the hot electron relaxation dynamics.** **a**, Snapshots of phonon excitation dynamics at 0.25, 0.5, 1.0 and 2.0 ps with  $E_{\text{ini}} = 1.0 \text{ eV}$ . **b,c**, Time evolution of the excited phonon number (**b**) and the total phonon energy (**c**) during the hot electron relaxation with  $E_{\text{ini}} = 1.0 \text{ eV}$ . **d**, Snapshots of the phonon excitation dynamics at 25, 50, 75 and 100 ps with  $E_{\text{ini}} = 0.1 \text{ eV}$ . **e,f**, Time evolution of the excited phonon number (**e**) and

the total phonon energy (**f**) during the hot electron relaxation with  $E_{\text{ini}} = 0.1 \text{ eV}$ . The dots sizes in **a** and **d** are proportional to the excited phonon number. The dots colors in **a–f** represent different phonon modes, and share the same legend as **g**. **g**, The eigenvectors for phonon mode  $E_{2g}$  at the  $\Gamma$  point, mode  $A_1$  at the  $K$  point, the longitudinal acoustic (LA) mode at the  $\Gamma$  point, and the transverse acoustic (TA) at the  $\Gamma$  point. **g**, The blue balls represent carbon atoms.

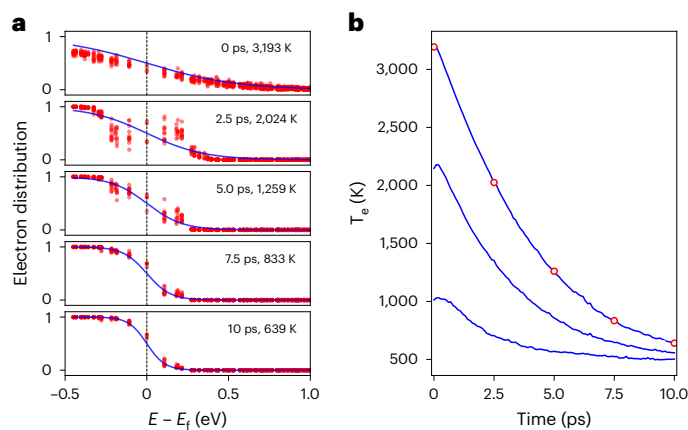


**Fig. 4 | Electron temperature evolution in graphene.** **a**, Snapshots of electron distribution at 0, 2.5, 5.0, 7.5 and 10 ps in multi-electron simulation with initial temperature of 3,000 K. **b**, Evolution of electron temperature for initial temperature of 1,000, 2,000 and 3,000 K. The five subpanels in **a** correspond to the five small red circles in **b**.

## Experimental validation

The simulation by NAMD\_k can explain most important experimental results. The hot electron relaxation timescale and decrease in  $T_e$  is of the same magnitude as our results<sup>36–38</sup>. Different experimental groups reported that slow decay via acoustic phonons plays a role when  $E_{\text{ini}} < 0.2 \text{ eV}$  (refs. 38–41), whereas the hot electrons can efficiently scatter with the optical phonons when  $E_{\text{ini}} > 0.2 \text{ eV}$  (refs. 33,35,39,41). The strong coupling with the  $A_1$  and  $E_{2g}$  modes and the quantized energy-loss are particularly in good agreement with the report by Na and colleagues<sup>35</sup>.

## Comparing NAMD\_k to other methods

The momentum-resolved rt-TDDFT algorithms based on Erhenfest dynamics have been implemented by several groups<sup>42–46</sup>; however,

as discussed by Lian et al.<sup>42</sup> and Hu et al.<sup>47</sup>, the momentum-dependence ( $\mathbf{k}$ -dependence) is only related to the electron and hole. In the photoexcited charge carrier relaxation process, the momentum of the electron and hole cancel each other so that the momentum conservation is kept, and only phonons at the  $\Gamma$  point are involved. For example, Hu et al.<sup>47</sup> only observe the hot carrier relaxation couple with the  $E_{2g}$  mode, which is located at the  $\Gamma$  point. For the NAMD\_r approach combined with time-dependent Kohn–Sham with a single-particle picture, only the  $\Gamma$  point is included for both the electron and phonon. An approach in which NAMD\_r was combined with GW plus the real-time Bethe–Salpeter equation (GW + rt-BSE) was recently developed for exciton dynamics<sup>20</sup>. As both electrons and holes are considered, the  $\mathbf{k}$ -dependence of electron and hole can be included, similar to rt-TDDFT based on Erhenfest dynamics; however, it also only includes the  $\Gamma$  point phonons. NAMD\_k provides a tool for charge carrier dynamics with both the  $\mathbf{k}$ -dependence for the electron and the  $\mathbf{q}$ -dependence for the phonon.

Compared with NAMD\_r, the NAMD\_k method not only gives consistent results, as is shown in Fig. 5 and discussed in the Methods section. Besides, NAMD\_k has other substantial advantages in treating solid state systems. First, the  $|\psi_{nk}(\mathbf{r}; \mathbf{R}_0)\rangle$  basis sets used here can be understood as diabatic basis sets, that is, each electronic state has a clear notion of band index and momentum. We do not need to reorder the electronic states when they cross each other; thus, the well-known state-crossing problem in surface hopping can be avoided<sup>48–52</sup>. Second, in the NAMD\_k method, the e–ph coupling can be understood in the time domain. Especially, the time-dependent phonon excitation induced by electron relaxation can be achieved, which is helpful to understand the photoexcitation-induced lattice structure distortion. But we can not calculate the time-dependent phonon excitation by the NAMD\_r method using CPA because the lattice distortion is predetermined by the AIMD simulation<sup>3,16</sup>. Taking graphene as an example, one can perform a molecular dynamics simulation using the phonon excitation at 2 ps as an initial condition to see how the lattice structure distorts after the hot electron transfers its energy to the lattice. It also provides a dynamical picture of the energy transport between the

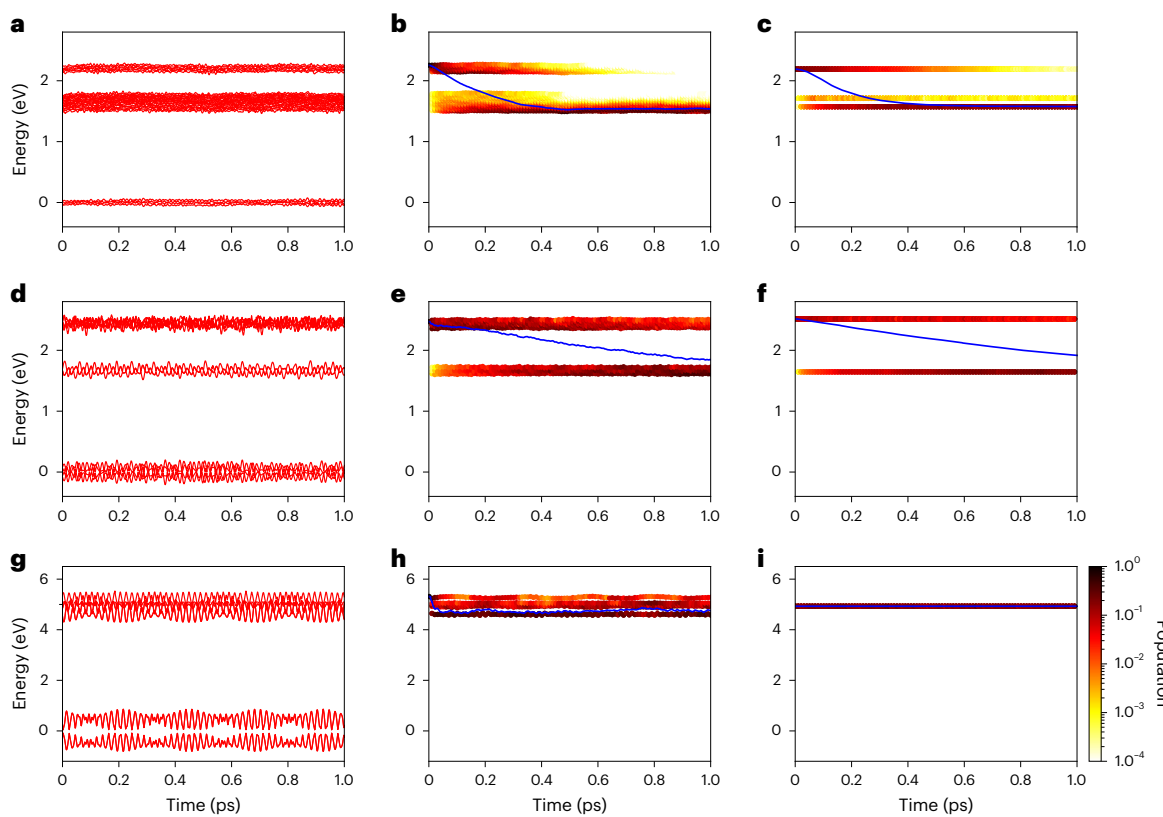


**Fig. 5 | Comparison of NAMD\_r and NAMD\_k simulations.** **a,d,g,** Energy evolution of Kohn–Sham states in the NAMD\_r approach with  $9 \times 9 \times 1$  (**a**),  $6 \times 6 \times 1$  (**d**) and  $3 \times 3 \times 1$  (**g**) supercells. **b,e,h,** The hot electron relaxation simulation using the NAMD\_r method with  $9 \times 9 \times 1$  (**b**),  $6 \times 6 \times 1$  (**e**) and  $3 \times 3 \times 1$  (**h**) supercells.

**c,f,i,** The hot electron relaxation simulation using NAMD\_k method with  $9 \times 9 \times 1\mathbf{k}$ - (**c**),  $6 \times 6 \times 1\mathbf{k}$ - (**f**) and a  $3 \times 3 \times 1\mathbf{k}$ - (**i**) point grids. The colored dots indicate the normalized electron population in different states, whereas the blue line represents the averaged electron energy.

electron and the phonon subsystems at the ab initio level beyond the semi-classical two-temperature model<sup>38,53</sup>.

Our work also agrees with the theoretical study by Bernardi et al.<sup>8</sup> based on the quasi-classical rt-BTE. It can be noted that hot electron relaxation mainly excites the  $A_1$ ,  $E_{2g}$ , longitudinal and transverse acoustic modes. All of these phonons are in-plane modes. The out-of-plane phonon modes are not directly excited, and we therefore propose that the buckling of graphene requires a phonon–phonon interaction, which can be studied by the rt-BTE method<sup>8</sup>. It is noted that the rt-BTE can also be used to study the real-time charge carrier and phonon dynamics<sup>8</sup>. Rt-BTE is based on the Boltzmann equation, which is valid under the semi-classical assumptions for charge transport. The charge carrier is described as a semi-classical quasi-particle and the quantum effects are incorporated based on the effective mass approximation. The Born approximation for the collisions, in the limit of perturbation for the e–ph interaction and instantaneous collisions is applied<sup>56</sup>. There are no memory effects in rt-BTE<sup>8</sup>. The NAMD\_k approach is based on the TDSE; the quantum character of the charge carrier is thus directly simulated. The dynamics of the charge carrier can be understood in a non-perturbative way. The memory effects are included in real-time propagation of TDSE, where the coefficients at a current time are correlated with the coefficients in the past. We propose that NAMD\_k is a quantum dynamics approach for charge carriers, whereas the semi-classical rt-BTE approach has the advantage to simulate the phonon dynamics, which usually occurs on a much longer timescale.

## Discussion

Beyond e–ph coupling based on the work by Bernardi and colleagues, the exciton–phonon coupling can be understood as a quantum superposition of the e–ph coupling contributed by the electron and hole<sup>20</sup>.

They also developed an approach for exciton dynamics in momentum space under the framework of rt-BTE<sup>54</sup>. Based on the work of exciton–phonon coupling and the GW + rt-BSE approach<sup>20</sup>, the NAMD\_k method can be extended for the investigation of exciton dynamics. Furthermore, the e–ph coupling can be calculated using the spinor basis sets, in which the SOC is included<sup>24</sup>. Thus NAMD\_k can also be used to study the SOC promoted spin dynamics.

NAMD\_k may also be applied to study indirect electron–hole (e–h) recombination and interband carrier relaxation; however, the current approach only includes the first order of e–ph coupling. When the band gap is larger than the phonon energy, the coupling of electrons to multiphonon through a higher order of e–ph coupling becomes important. The NAMD\_r approach naturally includes the higher-order of e–ph coupling. Furthermore, in the e–h recombination problem, usually only the valence band maximum and conduction band minimum need to be included, and a very dense of  $\mathbf{k}$ -point grid is not often required. The NAMD\_r approach is therefore usually more appropriate for the e–h recombination problem; however, if the momentum of the conduction band minimum and valence band maximum is very close to each other, for example, in the case of the Rashba effects induced momentum-dependent splitting<sup>55</sup>, the NAMD\_k has its advantage. Still, the future development of the NAMD\_k to include a higher order of e–ph coupling is essential for its application in e–h recombination problem. In Supplementary Section 6 we give an example of e–h recombination study in silicon bulk using the NAMD\_k and discuss its limitation.

The major approximation used in the NAMD\_k method is the harmonic approximation, which is applied to calculate the e–ph element  $g_{mn}(\mathbf{k}, \mathbf{q})$  and the time-dependent phonon population  $Q_{qv}(t)$ . Here we propose a possible stratagem to consider the anharmonic effects. The first step is using a different way to generate  $Q_{qv}(t)$ . For example,

a molecular dynamics simulation can be performed to generate the atomic nuclear  $\mathbf{R}(t)$ . Then  $Q_{qv}(t)$  can be obtained by Fourier transform from  $\mathbf{R}(t)$ . Of course, if molecular dynamics is used to get  $Q_{qv}(t)$ , a large supercell must be used to capture the phonons at different  $\mathbf{q}$ -points. But the advantage in NAMD\_k is that only  $Q_{qv}(t)$  is needed. The electronic wave function for each step is not required. Molecular dynamics simulations can therefore be performed using empirical or deep learning potentials, which makes the large supercell calculation realistic. One can also use the rt-BTE approach to get the time-resolved phonon population  $Q_{qv}(t)$ , where the phonon–phonon interaction is captured using perturbation theory<sup>8</sup>. The second step is to consider the anharmonic effects in the calculation of the e–ph coupling matrix element  $g_{mnv}(\mathbf{k}, \mathbf{q})$ , which can be expanded to higher order. The work to include the anharmonic effects in NAMD\_k is an interesting and important topic in the future.

## Methods

In the NAMD\_k approach, the NAC from the NAMD\_r approach is replaced with e–ph coupling by expanding the charge carrier wavefunction with the static Kohn–Sham orbitals of the equilibrium atomic configuration, which is the key point in the simulation of momentum space. To calculate the e–ph term, we expand the potential energy  $V(\mathbf{r}; \mathbf{R}(t))$  in terms of nuclear displacements  $\Delta\mathbf{R}(t)$ . The potential energy approximated to first order in displacements is

$$V(\mathbf{r}; \mathbf{R}(t)) = V(\mathbf{r}; \mathbf{R}_0) + \sum_{pa} \frac{\partial V(\mathbf{r}; \mathbf{R})}{\partial \mathbf{R}_{pa}} \Big|_{\mathbf{R}=\mathbf{R}_0} \cdot \Delta\mathbf{R}_{pa}(t), \quad (12)$$

where the position of the nucleus  $\alpha$  in the  $p$ th unit cell is denoted as  $\mathbf{R}_{pa} = \mathbf{L}_p + \mathbf{r}_\alpha$ , and  $\mathbf{L}_p$  is the cell vector. In practice, it is convenient to decompose nuclear displacements  $\Delta\mathbf{R}(t)$  into normal modes

$$\Delta\mathbf{R}_{pa}(t) = \sqrt{\frac{M_0}{NM_\alpha}} \sum_{qv} e^{i\mathbf{q} \cdot \mathbf{L}_p} \mathbf{e}_{av}(\mathbf{q}) Q_{qv}(t), \quad (13)$$

where  $N$  is the number of unit cells according to the Born–von Kármán boundary conditions,  $M_0$  is an arbitrary reference mass introduced to ensure that both sides of the equation have the dimension of length. Typically,  $M_0$  is chosen to be the proton mass;  $\mathbf{e}_{av}(\mathbf{q})$  is the polarization of the vibration wave corresponding to the wave vector  $\mathbf{q}$  and mode  $v$ ; and  $Q_{qv}(t)$  is the normal mode coordinate of the corresponding mode. According to equation (6),

$$\Delta V(\mathbf{r}; \mathbf{R}(t)) = \sqrt{\frac{1}{N}} \sum_{qv} \sum_{pa} \sqrt{\frac{M_0}{M_\alpha}} e^{i\mathbf{q} \cdot \mathbf{L}_p} \frac{\partial V(\mathbf{r}; \mathbf{R})}{\partial \mathbf{R}_{pa}} \Big|_{\mathbf{R}=\mathbf{R}_0} \cdot \mathbf{e}_{av}(\mathbf{q}) Q_{qv}(t). \quad (14)$$

Here, by defining

$$\partial_{qa} v(\mathbf{r}; \mathbf{R}_0) = \sum_p e^{-i\mathbf{q} \cdot (\mathbf{r} - \mathbf{L}_p)} \frac{\partial V(\mathbf{r}; \mathbf{R})}{\partial \mathbf{R}_{pa}} \Big|_{\mathbf{R}=\mathbf{R}_0}, \quad (15)$$

and

$$\Delta_{qv} v(\mathbf{r}; \mathbf{R}_0) = \sum_\alpha (M_0/M_\alpha)^{1/2} \partial_{qa} v(\mathbf{r}; \mathbf{R}_0) \cdot \mathbf{e}_{av}(\mathbf{q}) l_{qv}, \quad (16)$$

where  $l_{qv}$  is the zero-point displacement amplitude:

$$l_{qv} = \sqrt{\frac{\hbar}{2M_0 \omega_{qv}}} \quad (17)$$

One can show that  $\partial_{qa} v(\mathbf{r}; \mathbf{R}_0)$  and  $\Delta_{qv} v(\mathbf{r}; \mathbf{R}_0)$  are lattice-periodic functions. Equation (14) can then be written as

$$\Delta V(\mathbf{r}; \mathbf{R}(t)) = N^{-1/2} \sum_{qv} e^{i\mathbf{q} \cdot \mathbf{r}} \Delta_{qv} v(\mathbf{r}; \mathbf{R}_0) Q_{qv}(t) l_{qv}^{-1}. \quad (18)$$

By combining equations (9) and (18), we have

$$\begin{aligned} H_{mk', nk}^{e-ph} &= N^{-1/2} \sum_{qv} N^{-1} \langle u_{mk'} | e^{-i(k' - k - \mathbf{q}) \cdot \mathbf{r}} \Delta_{qv} v(\mathbf{r}; \mathbf{R}_0) | u_{nk} \rangle Q_{qv}(t) l_{qv}^{-1} \\ &= N^{-1/2} \sum_{qv} \langle u_{mk'} | \Delta_{qv} v(\mathbf{r}; \mathbf{R}_0) | u_{nk} \rangle_{uc} \delta_{q, k' - k} Q_{qv}(t) l_{qv}^{-1} \\ &= N^{-1/2} \sum_v g_{mnv}(\mathbf{k}, \mathbf{q}) Q_{qv}(t) l_{qv}^{-1} \Big|_{q=k'-k}, \end{aligned} \quad (19)$$

where  $u_{mk'}$  and  $u_{nk}$  are the periodic parts of Bloch's form of Kohn–Sham orbitals (see Supplementary equation (2)). The inner product in the first line is an integral over the entire Born–von Kármán supercell. Similar to the proof in Supplementary Section 1, one can show that the integral can be converted to an integral over the unit cell, provided that the momentum is conserved;  $g_{mnv}(\mathbf{k}, \mathbf{q})$  is referred to as the e–ph matrix element

$$g_{mnv}(\mathbf{k}, \mathbf{q}) = \langle u_{mk+q} | \Delta_{qv} v(\mathbf{r}; \mathbf{R}_0) | u_{nk} \rangle_{uc}. \quad (20)$$

As we obtain the e–ph coupling Hamiltonian in equation (10), we can calculate time-dependent coefficient evolution of excited carrier by equation (7). We then simulate the carrier dynamics using the FSSH method based on the time-dependent coefficients. The FSSH method represents a time-evolving electron–nuclear system by an ensemble of trajectories, propagating under the influence of deterministic (via the TDSE) and stochastic (via surface hopping) factors. Evolution of the system of interest is defined in a joint space combining classical phase-space for nuclei and discrete quantum states for electrons. The paths are constructed such that the FSSH probabilities for all states at all times—averaged over the trajectory ensemble—are equal to the corresponding probabilities obtained from the TDSE. The hopping probability are given by diagonal elements of the density matrix:

$$\rho_{mk', nk}(t) = c_{mk'}^*(t) c_{nk}(t). \quad (21)$$

The off-diagonal elements determine the probabilities of transitions between electronic states. For simplicity, we take the diagonal elements  $\rho_{nk, nk}$  as  $\rho_{nk}$ . If the system is in state  $nk$  at time  $t$ , then the probability to leave this state at time  $t + \Delta t$  is:

$$P_{nk}(t; t + \Delta t) = \frac{\rho_{nk}(t) - \rho_{nk}(t + \Delta t)}{\rho_{nk}(t)} = -\frac{\int_t^{t+\Delta t} \dot{\rho}_{nk}(t) dt}{\rho_{nk}(t)}. \quad (22)$$

From the definition of the density matrix, and from the TDSE, it follows that:

$$\dot{\rho}_{nk}(t) = \sum_{mk'} -\frac{2}{\hbar} \text{Im} \left( \rho_{mk', nk}^* H_{mk', nk}^{e-ph} \right). \quad (23)$$

Splitting the resulting hopping probability into various channels,  $mk'$ , one obtains the probability of transition between the pair of states  $nk \rightarrow mk'$ :

$$P_{nk \rightarrow mk'}(t; t + \Delta t) = \frac{2}{\hbar} \frac{\int_t^{t+\Delta t} \text{Im} \left( \rho_{mk', nk}^* H_{mk', nk}^{e-ph} \right) dt}{\rho_{nk}(t)}. \quad (24)$$

Note that each transition from  $nk$  to  $mk'$  corresponds to one e–ph scattering process, where the energy and crystal momentum must be conserved; however, equation (24) cannot guarantee the conservation law. To explicitly introduce the conservation law into the probability equation, recall that Fermi's golden rule gives the transition rate between two states

$$\begin{aligned} \frac{d}{dt} P_{nk \rightarrow mk'}(t) &= \frac{2\pi}{\hbar} |H_{mk', nk}^{e-ph}|^2 \times [ \delta(\epsilon_{mk'} - \epsilon_{nk} - \hbar\omega_{qv}) \\ &\quad + \delta(\epsilon_{mk'} - \epsilon_{nk} + \hbar\omega_{qv}) ]. \end{aligned} \quad (25)$$

As a result, the modified hopping probability equation changes to

$$\tilde{P}_{n\mathbf{k} \rightarrow m\mathbf{k}'}(t; t + \Delta t) = \frac{2}{\hbar} \frac{\text{Im} \left( \rho_{m\mathbf{k}', n\mathbf{k}}^*(t) \tilde{H}_{m\mathbf{k}', n\mathbf{k}}^{\text{e-ph}} \right) \Delta t}{\rho_{n\mathbf{k}}(t)}, \quad (26)$$

where  $\tilde{H}_{m\mathbf{k}', n\mathbf{k}}^{\text{e-ph}}$  is given by

$$\tilde{H}_{m\mathbf{k}', n\mathbf{k}}^{\text{e-ph}} = \frac{2\pi}{N} \sum_{\mathbf{q}} |g_{mn\mathbf{v}}(\mathbf{k}, \mathbf{q})|^2 (n_{\mathbf{q}\mathbf{v}} + \frac{1}{2}) \times [\delta(\epsilon_{m\mathbf{k}'} - \epsilon_{n\mathbf{k}} - \hbar\omega_{\mathbf{q}\mathbf{v}}) + \delta(\epsilon_{m\mathbf{k}'} - \epsilon_{n\mathbf{k}} + \hbar\omega_{\mathbf{q}\mathbf{v}})]. \quad (27)$$

where the two  $\delta$  function correspond to absorbtion and emission of the phonon, respectively; however, in practical implementation, a Gaussian function with certain broadening  $\sigma$  is used to approximate the Dirac  $\delta$ -function

$$\delta(E) \approx \frac{1}{\sigma\sqrt{2\pi}} e^{-\frac{E^2}{2\sigma^2}}. \quad (28)$$

If the computed probability is negative, it is reset to zero. Thus, in general, the FSSH assigns a probability for transition from the current electronic state  $n\mathbf{k}$  to the new state  $m\mathbf{k}'$ , as:

$$g_{n\mathbf{k} \rightarrow m\mathbf{k}'}(t; t + \Delta t) = \max [0, \tilde{P}_{n\mathbf{k} \rightarrow m\mathbf{k}'}(t; t + \Delta t)], \quad (29)$$

$$g_{n\mathbf{k} \rightarrow n\mathbf{k}}(t; t + \Delta t) = 1 - \sum_{m\mathbf{k}' \neq n\mathbf{k}} g_{n\mathbf{k} \rightarrow m\mathbf{k}'}(t; t + \Delta t). \quad (30)$$

To reflect the detailed balance condition, the hop rejection and velocity rescaling of the standard FSSH are replaced in the FSSH-CPA by scaling the transition probabilities  $g_{n\mathbf{k} \rightarrow n\mathbf{k}}$  with the Boltzmann factor:

$$g_{n\mathbf{k} \rightarrow m\mathbf{k}'} \Rightarrow g_{n\mathbf{k} \rightarrow m\mathbf{k}'} b_{n\mathbf{k} \rightarrow m\mathbf{k}'}, \quad (31)$$

$$b_{n\mathbf{k} \rightarrow m\mathbf{k}'} = \begin{cases} \exp\left(-\frac{\epsilon_{m\mathbf{k}'} - \epsilon_{n\mathbf{k}}}{k_B T}\right) & \epsilon_{m\mathbf{k}'} > \epsilon_{n\mathbf{k}} \\ 1 & \epsilon_{m\mathbf{k}'} \leq \epsilon_{n\mathbf{k}} \end{cases}. \quad (32)$$

After calculating the transition probability between any two states, we can perform simulation of carrier dynamics using the FSSH-CPA strategy, as discussed by Akimov and co-workers<sup>16</sup>.

To verify the validity of the NAMD\_k method, we compare the calculation results of the NAMD\_k and NAMD\_r approaches. In the NAMD\_r approach, a supercell is required to sample the phonon excitation with different  $\mathbf{q}$ -points. Here we only simulate  $9 \times 9 \times 1$ ,  $6 \times 6 \times 1$  and  $3 \times 3 \times 1$  supercell due to the limitation of computational cost. We then compare the results with what NAMD\_k obtains using  $9 \times 9 \times 1$ ,  $6 \times 6 \times 1$  and  $3 \times 3 \times 1$  k-point grid, respectively (see Fig. 5 for the results). As the k-point grid is not dense enough, there are energy gaps in all three systems. We simulate the hot electron relaxation with  $E_{\text{ini}} = 2.2$ ,  $2.5$  and  $5.1$  eV for the three systems, respectively. The  $\sigma$  value used in NAMD\_k is estimated from the energy level oscillation in the NAMD\_r simulation, which can be seen from Fig. 5a,d,j. One can see that the NAMD\_r and NAMD\_k approaches achieve very similar results, proving the validity of the NAMD\_k approach. Due to the existing of energy gaps, the hot electron can not relax close to  $E_f$  within  $1.0$  ps, suggesting that a dense k-point grid is required to simulate the hot electron relaxation in graphene.

The computational cost of NAMD\_k is notably smaller than that of NAMD\_r. The work flow of NAMD\_r includes: (1) molecular dynamics simulation; (2) Kohn-Sham wavefunction and NAC calculation; and (3) NAMD simulation. The major computational cost comes from steps 1 and 2. Step 3 depends on the number of electronic states included and is typically negligible under the CPA approximation. Taking  $9 \times 9 \times 1$  graphene supercell as an example, if we perform a 5 ps molecular dynamics

**Table 1 | Comparisons in computational cost**

Supercell/k-point grid	NAMD_r (h)	NAMD_k (h)
$3 \times 3 \times 1$	1.2	0.4
$6 \times 6 \times 1$	7.7	1.1
$9 \times 9 \times 1$	39.6	2.0
$150 \times 150 \times 1$	$10^6$ (estimated)	13.2

The computational time (in hours) of NAMD\_r and NAMD\_k for  $3 \times 3 \times 1$ ,  $6 \times 6 \times 1$ ,  $9 \times 9 \times 1$ , and  $150 \times 150 \times 1$  supercell or k-point grid using 48 cores on a single Intel(R) Gold 6240R @ 2.40GHz CPU.

and a 2 ps NAMD, it will take 39.6 h using 48 cores on a single Intel(R) Gold 6240R @ 2.40GHz CPU. The workflow of NAMD\_k includes: (1) e-ph coupling elements; and (2) NAMD simulation. For e-ph coupling elements (step 1), the computational cost depends on the size of the unit cell. In the case of graphene, the e-ph calculation takes 7.2 h for  $150 \times 150 \times 1$  k-point grid if 48 cores are used. The length of the NAMD simulation (step 2) depends on the number of electronic states. If we use  $9 \times 9 \times 1$  k-point grid, the relaxation for 2 ps simulation takes around 28 s to sample  $10^4$  trajectories, which can be neglected. But if we use  $150 \times 150 \times 1$  k-point grid, we have much more electronic states and it takes 6 h. There is still lots of room to optimize the NAMD part in NAMD\_k. In spite of this, for NAMD\_k the total computational time for graphene with  $150 \times 150 \times 1$  k-point grid is 13.2 h using 48 cores, which is less than one-third compared with NAMD\_r with a  $9 \times 9 \times 1$  supercell. In Table 1 we have summarized the computational cost of NAMD\_r and NAMD\_k with different supercells and k-point grids. One can see the NAMD\_k is always more efficient than NAMD\_r. The advantages of NAMD\_k become more substantial for denser k-point grid, which corresponds to a larger supercell in NAMD\_r. If we compare with the NAMD\_r simulation with a  $150 \times 150 \times 1$  supercell, whose computational time is too long to execute and is estimated to be about  $10^6$  h, which is  $10^5$  longer than that of the NAMD\_k simulation.

## Data availability

These data are obtained by NAMD\_k simulations using our homemade code<sup>56,57</sup>. The source data for Figs. 1–5, Supplementary Figs. 1–3 and input files for NAMD\_k simulations have been deposited in the Materials Cloud Archive at <https://doi.org/10.24435/materialscloud:2n-3j>. Source Data are provided with this paper.

## Code availability

The code for our algorithm and a guide to reproducing the results is available at GitHub<sup>56</sup> and Code Ocean<sup>57</sup>. In the calculation, e-ph coupling is calculated by the package Perturbo<sup>58</sup>, which can be obtained at <https://perturbo-code.github.io>.

## References

- Tisdale, W. A. et al. Hot-electron transfer from semiconductor nanocrystals. *Science* **328**, 1543–1547 (2010).
- Akimov, A. V., Neukirch, A. J. & Prezhdo, O. V. Theoretical insights into photoinduced charge transfer and catalysis at oxide interfaces. *Chem. Rev.* **113**, 4496–4565 (2013).
- Zheng, Q. et al. Ab initio nonadiabatic molecular dynamics investigations on the excited carriers in condensed matter systems. *WIREs Comput. Mol. Sci.* **9**, 1411 (2019).
- Sobota, J. A., He, Y. & Shen, Z.-X. Angle-resolved photoemission studies of quantum materials. *Rev. Modern Phys.* **93**, 025006 (2021).
- Poncé, S., Li, W., Reichardt, S. & Giustino, F. First-principles calculations of charge carrier mobility and conductivity in bulk semiconductors and two-dimensional materials. *Rep. Prog. Phys.* **83**, 036501 (2020).

6. Bernardi, M. First-principles dynamics of electrons and phonons\*. *Eur. Phys. J. B* **89**, 239 (2016).
7. Jhalani, V. A., Zhou, J.-J. & Bernardi, M. Ultrafast hot carrier dynamics in gan and its impact on the efficiency droop. *Nano Lett.* **17**, 5012–5019 (2017).
8. Tong, X. & Bernardi, M. Toward precise simulations of the coupled ultrafast dynamics of electrons and atomic vibrations in materials. *Phys. Rev. Res.* **3**, 023072 (2021).
9. Li, X., Tully, J. C., Schlegel, H. B. & Frisch, M. J. Ab initio ehrenfest dynamics. *J. Chem. Phys.* **123**, 084106 (2005).
10. Meng, S. & Kaxiras, E. Real-time, local basis-set implementation of time-dependent density functional theory for excited state dynamics simulations. *J. Chem. Phys.* **129**, 054110 (2008).
11. Kolesov, G., Granas, O., Hoyt, R., Vinichenko, D. & Kaxiras, E. Real-time TD-DFT with classical ion dynamics: methodology and applications. *J. Chem. Theory Comput.* **12**, 466–476 (2016).
12. Wang, Z., Li, S.-S. & Wang, L.-W. Efficient real-time time-dependent density functional theory method and its application to a collision of an ion with a 2D material. *Phys. Rev. Lett.* **114**, 063004 (2015).
13. Runge, E. & Gross, E. K. U. Density-functional theory for time-dependent systems. *Phys. Rev. Lett.* **52**, 997–1000 (1984).
14. Schleife, A., Draeger, E. W., Kanai, Y. & Correa, A. A. Plane-wave pseudopotential implementation of explicit integrators for time-dependent Kohn-Sham equations in large-scale simulations. *J. Chem. Phys.* **137**, 22–546 (2012).
15. Shepard, C., Zhou, R., Yost, D. C., Yao, Y. & Kanai, Y. Simulating electronic excitation and dynamics with real-time propagation approach to TDDFT within plane-wave pseudopotential formulation. *J. Chem. Phys.* **155**, 100901 (2021).
16. Akimov, A. V. & Prezhdo, O. V. The pyxaid program for non-adiabatic molecular dynamics in condensed matter systems. *J Chem. Theory Comput.* **9**, 4959–72 (2013).
17. Tully, J. C. Molecular dynamics with electronic transitions. *J. Chem. Phys.* **93**, 1061–1071 (1990).
18. Cui, G. & Thiel, W. Generalized trajectory surface-hopping method for internal conversion and intersystem crossing. *J. Chem. Phys.* **141**, 124101 (2014).
19. Zhang, X., Li, Z. & Lu, G. First-principles determination of charge carrier mobility in disordered semiconducting polymers. *Phys. Rev. B* **82**, 205210 (2010).
20. Jiang, X. et al. Real-time GW-BSE investigations on spin-valley exciton dynamics in monolayer transition metal dichalcogenide. *Sci. Adv.* **7**, 3759 (2021).
21. Liu, J., Zhang, X. & Lu, G. Excitonic effect drives ultrafast dynamics in van der waals heterostructures. *Nano Lett.* **20**, 4631–4637 (2020).
22. Zheng, Q. et al. Phonon-assisted ultrafast charge transfer at van der waals heterostructure interface. *Nano Lett.* **17**, 6435–6442 (2017).
23. Li, W., Zhou, L., Prezhdo, O. V. & Akimov, A. V. Spin-orbit interactions greatly accelerate nonradiative dynamics in lead halide perovskites. *ACS Energy Lett.* **3**, 2159–2166 (2018).
24. Zheng, Z., Zheng, Q. & Zhao, J. Spin-orbit coupling induced demagnetization in Ni: ab initio nonadiabatic molecular dynamics perspective. *Phys. Rev. B* **105**, 085142 (2022).
25. Liu, X.-Y. et al. Spin-orbit coupling accelerates the photoinduced interfacial electron transfer in a fullerene-based perovskite heterojunction. *J. Phys. Chem. Lett.* **12**, 1131–1137 (2021).
26. Sohier, T., Calandra, M. & Mauri, F. Density functional perturbation theory for gated two-dimensional heterostructures: theoretical developments and application to flexural phonons in graphene. *Phys. Rev. B* **96**, 075448 (2017).
27. Monserrat, B. Electron-phonon coupling from finite differences. *J. Phys. Condensed Matter* **30**, 083001 (2018).
28. Ye, Z.-Q., Cao, B.-Y., Yao, W.-J., Feng, T. & Ruan, X. Spectral phonon thermal properties in graphene nanoribbons. *Carbon* **93**, 915–923 (2015).
29. Dal Conte, S. et al. Snapshots of the retarded interaction of charge carriers with ultrafast fluctuations in cuprates. *Nat. Phys.* **11**, 421–426 (2015).
30. Park, C.-H., Giustino, F., Cohen, M. L. & Louie, S. G. Velocity renormalization and carrier lifetime in graphene from the electron-phonon interaction. *Phys. Rev. Lett.* **99**, 086804 (2007).
31. Park, C.-H., Giustino, F., Cohen, M. L. & Louie, S. G. Electron-phonon interactions in graphene, bilayer graphene, and graphite. *Nano Lett.* **8**, 4229–4233 (2008).
32. Gierz, I. et al. Snapshots of non-equilibrium dirac carrier distributions in graphene. *Nat. Mater.* **12**, 1119–1124 (2013).
33. Johannsen, J. C. et al. Direct view of hot carrier dynamics in graphene. *Phys. Rev. Lett.* **111**, 027403 (2013).
34. Gierz, I. et al. Tracking primary thermalization events in graphene with photoemission at extreme time scales. *Phys. Rev. Lett.* **115**, 086803 (2015).
35. Na, M. X. et al. Direct determination of mode-projected electron-phonon coupling in the time domain. *Science* **366**, 1231 (2019).
36. Kampfrath, T., Perfetti, L., Schapper, F., Frischkorn, C. & Wolf, M. Strongly coupled optical phonons in the ultrafast dynamics of the electronic energy and current relaxation in graphite. *Phys. Rev. Lett.* **95**, 187403 (2005).
37. Stange, A. et al. Hot electron cooling in graphite: supercollision versus hot phonon decay. *Phys. Rev. B* **92**, 184303 (2015).
38. Wang, H. et al. Ultrafast relaxation dynamics of hot optical phonons in graphene. *Appl. Phys. Lett.* **96**, 081917 (2010).
39. Butscher, S., Milde, F., Hirtschulz, M., Malić, E. & Knorr, A. Hot electron relaxation and phonon dynamics in graphene. *Appl. Phys. Lett.* **91**, 203103 (2007).
40. Strait, J. H. et al. Very slow cooling dynamics of photoexcited carriers in graphene observed by optical-pump terahertz-probe spectroscopy. *Nano Lett.* **11**, 4902–4906 (2011).
41. Zhang, H. et al. Self-energy dynamics and the mode-specific phonon threshold effect in Kekulé-ordered graphene. *Natl Sci. Rev.* **9**, 175 (2022).
42. Lian, C., Hu, S.-Q., Guan, M.-X. & Meng, S. Momentum-resolved TDDFT algorithm in atomic basis for real time tracking of electronic excitation. *J. Chem. Phys.* **149**, 154104 (2018).
43. Bertsch, G. F., Iwata, J.-I., Rubio, A. & Yabana, K. Real-space, real-time method for the dielectric function. *Phys. Rev. B* **62**, 7998–8002 (2000).
44. Marques, M. A. L., Castro, A., Bertsch, G. F. & Rubio, A. octopus: a first-principles tool for excited electron-ion dynamics. *Comput. Phys. Commun.* **151**, 60–78 (2003).
45. Castro, A. et al. octopus: a tool for the application of time-dependent density functional theory. *Phys. Status Solidi B* **243**, 2465–2488 (2006).
46. Andrade, X. et al. Real-space grids and the octopus code as tools for the development of new simulation approaches for electronic systems. *Phys. Chem. Chem. Phys.* **17**, 31371–31396 (2015).
47. Hu, S.-Q. et al. Tracking photocarrier-enhanced electron-phonon coupling in nonequilibrium. *npj Quantum Mater.* **7**, 14 (2022).
48. Chu, W. & Prezhdo, O. V. Concentric approximation for fast and accurate numerical evaluation of nonadiabatic coupling with projector augmented-wave pseudopotentials. *J. Phys. Chem. Lett.* **12**, 3082–3089 (2021).

49. Chu, W. et al. Accurate computation of nonadiabatic coupling with projector augmented-wave pseudopotentials. *J. Phys. Chem. Lett.* **11**, 10073–10080 (2020).
50. Fernandez-Alberti, S., Roitberg, A. E., Nelson, T. & Tretiak, S. Identification of unavoided crossings in nonadiabatic photoexcited dynamics involving multiple electronic states in polyatomic conjugated molecules. *J. Chem. Phys.* **137**, 014512 (2012).
51. Qiu, J., Bai, X. & Wang, L. Crossing classified and corrected fewest switches surface hopping. *J. Phys. Chem. Lett.* **9**, 4319–4325 (2018).
52. Wang, L. & Prezhdo, O. V. A simple solution to the trivial crossing problem in surface hopping. *J. Phys. Chem. Lett.* **5**, 713–719 (2014).
53. Hale, P. J., Hornett, S. M., Moger, J., Horsell, D. W. & Hendry, E. Hot phonon decay in supported and suspended exfoliated graphene. *Phys. Rev. B* **83**, 121404 (2011).
54. Chen, H.-Y., Sangalli, D. & Bernardi, M. Exciton-phonon interaction and relaxation times from first principles. *Phys. Rev. Lett.* **125**, 107401 (2020).
55. Zheng, F., Tan, L. Z., Liu, S. & Rappe, A. M. Rashba spin-orbit coupling enhanced carrier lifetime in  $\text{CH}_3\text{NH}_3\text{PbI}_3$ . *Nano Lett.* **15**, 7794–7800 (2015).
56. Zheng, Z. & Zheng, Q. Hefei-NAMD-EPC v.1.10.6 (GitHub, 2023); <https://github.com/ZhenfaZheng/NAMDinMomentumSpace.git>
57. Zheng, Z. & Zheng, Q. Ab initio real-time quantum dynamics of charge carriers in momentum space. *CodeOcean* <https://doi.org/10.24433/CO.4619996.v1> (2023).
58. Zhou, J.-J. et al. Perturbo: A software package for ab initio electron–phonon interactions, charge transport and ultrafast dynamics. *Comput. Phys. Commun.* <https://doi.org/10.1016/j.cpc.2021.107970> (2021).

## Acknowledgements

J.Z. acknowledges the support of the Innovation Program for Quantum Science and Technology (grant no. 2021ZD0303306); the National Natural Science Foundation of China (NSFC, grant nos. 12125408 and 11974322); and the informatization plan of Chinese Academy of Sciences (grant no. CAS-WX2021SF-0105). Q.Z. acknowledges the support of the NSFC (grant no. 12174363). O.V.P. acknowledges funding of the US National Science Foundation (grant no. CHE-2154367). Calculations were performed at the Hefei Advanced Computing Center, the Supercomputing Center at USTC, and the ORISE Supercomputer. We received no specific funding for this work.

## Author contributions

Y.S. contributed to this work before March 2022. J.Z. supervised the research project. Y.S. conceived the original idea. J.Z., Q.Z., Y.S. and Z.Z. developed the method, whereas J.-J.Z. and O.V.P. provided suggestions to improve the method. Q.Z. constructed the original Hefei-NAMD code. Z.Z. developed the NAMD\_\*\*k\*\* version of Hefei-NAMD on the basis of the original Hefei-NAMD code, performed the NAMD\_\*\*k\*\* simulation of graphene, and data analysis, with help from Q.Z. J.-J.Z. provided the patch of PERTURBO package for outputting e–ph matrix elements data. J.Z., Q.Z. and Z.Z. wrote the manuscript. The manuscript reflects the contributions of all authors.

## Competing interests

The authors declare no competing interests.

## Additional information

**Supplementary information** The online version contains supplementary material available at <https://doi.org/10.1038/s43588-023-00456-9>.

**Correspondence and requests for materials** should be addressed to Yongliang Shi, Qijing Zheng or Jin Zhao.

**Peer review information** *Nature Computational Science* thanks Jun Yin, Sergei Tretiak, and the other, anonymous, reviewer(s) for their contribution to the peer review of this work. Primary Handling Editor: Jie Pan, in collaboration with the *Nature Computational Science* team.

**Reprints and permissions information** is available at [www.nature.com/reprints](http://www.nature.com/reprints).

**Publisher's note** Springer Nature remains neutral with regard to jurisdictional claims in published maps and institutional affiliations.

Springer Nature or its licensor (e.g. a society or other partner) holds exclusive rights to this article under a publishing agreement with the author(s) or other rightsholder(s); author self-archiving of the accepted manuscript version of this article is solely governed by the terms of such publishing agreement and applicable law.

© The Author(s), under exclusive licence to Springer Nature America, Inc. 2023